

The role of C/O in nitrile astrochemistry in PDRs and planet-forming disks

ROMANE LE GAL,¹ MADISON T. BRADY,^{2,*} KARIN I. ÖBERG,¹ EVELYNE ROUEFF,³ AND FRANCK LE PETIT³

¹*Harvard-Smithsonian Center for Astrophysics, 60 Garden St., Cambridge, MA 02138, USA*

²*California Institute of Technology, Pasadena, CA 91125, USA*

³*Sorbonne Université, Observatoire de Paris, Université PSL, CNRS, LERMA, F-92190, Meudon, France*

(Received July 30th, 2019; Revised October 1st, 2019; Accepted October 2nd, 2019)

ABSTRACT

Complex nitriles, such as HC₃N, and CH₃CN, are observed in a wide variety of astrophysical environments, including at relatively high abundances in photon-dominated regions (PDR) and the UV exposed atmospheres of planet-forming disks. The latter have been inferred to be oxygen-poor, suggesting that these observations may be explained by organic chemistry in C-rich environments. In this study we first explore if the PDR complex nitrile observations can be explained by gas-phase PDR chemistry alone if the elemental C/O ratio is elevated. In the case of the Horsehead PDR, we find that gas-phase chemistry with C/O \gtrsim 0.9 can indeed explain the observed nitrile abundances, increasing predicted abundances by several orders of magnitude compared to standard C/O assumptions. We also find that the nitrile abundances are sensitive to the cosmic ray ionization treatment, and provide constraints on the branching ratios between CH₃CN and CH₃NC productions. In a fiducial disk model, an elevated C/O ratio increases the CH₃CN and HC₃N productions by more than an order of magnitude, bringing abundance predictions within an order of magnitude to what has been inferred from observations. The C/O ratio appears to be a key variable in predicting and interpreting complex organic molecule abundances in photon-dominated regions across a range of scales.

Keywords: astrochemistry – ISM: molecules – methods: numerical – photon-dominated region (PDR) – protoplanetary disks

1. INTRODUCTION

Origins of life on Earth must have been closely linked to the emergence of information-rich polymers such as DNA (deoxyribonucleic acid) or RNA (ribonucleic acid). While their initial formation on the early Earth remains mysterious, there are plausible chemical pathways to their building blocks on the early Earth through a nitrile-centered UV-driven chemistry (Powner et al. 2009; Patel et al. 2015; Sutherland 2016). Simple and complex nitriles are abundantly found at all stages of star and planet formation, including in planet-forming disks, suggesting that the organic chemistry that preceded life on Earth is not unique to the Solar System (Chapillon et al. 2012; Öberg et al. 2015; Bergner et al.

2018; Loomis et al. 2018). Perhaps surprisingly CH₃CN and HC₃N are two of the most commonly detected larger organic molecules in disks, and the origins of these high abundances are uncertain. Öberg et al. (2015) and Loomis et al. (2018) both invoke grain-surface chemical pathways to predict sufficient amounts of CH₃CN, but these predictions are extremely uncertain due to lack of experimental data on ice nitrile chemistry and desorption.

One important observational constraint is that observed HC₃N and CH₃CN emissions appear to come from the upper most layer of disks or disk atmospheres (Öberg et al. 2015; Bergner et al. 2018; Loomis et al. 2018). Disk atmospheres are proposed analogs to the more well-studied photon-dominated regions (PDR). Interestingly, complex nitriles have also been detected at unexpectedly high abundances in the deeply characterized PDR, the Horsehead nebula (Gratier et al. 2013). Located in the Orion constellation and seen almost edge-on (Abergel et al. 2003), the Horsehead nebula consti-

Corresponding author: Romane Le Gal
romane.le_gal@cfa.harvard.edu

* Noland Internship at Harvard-Smithsonian Center for Astrophysics (summer 2018)

tutes a perfect template source to study in detail the physics and chemistry occurring in PDRs. With the WHISPER survey¹ (Wideband High-resolution Iram-30m Survey at two Positions with Emir Receivers, PI: J. Pety), the chemistry of this PDR has been surveyed at unprecedented detail, both at the edge of the PDR (defined by the HCO peak emission, Gerin et al. 2009), and toward an interior ‘core’ position (defined by the DCO⁺ peak, Pety et al. 2007). Of interest to this study, Gratier et al. (2013) found that the CH₃CN emission is ~ 40 times brighter at the PDR position than in the ‘Core’. Similar to protoplanetary disks, this excess in CH₃CN could not be explained by gas-phase chemistry alone, and Gratier et al. (2013) instead suggested that a combination of UV-mediated surface chemistry with surface desorption processes were responsible. However, models developed by Le Gal et al. (2017), coupling the Meudon PDR (Le Bourlot et al. 1993; Le Petit et al. 2006; Le Bourlot et al. 2012) and the Nautilus (Hersant et al. 2009; Ruaud et al. 2016) astrochemical codes, could not reproduce the abundance of CH₃CN at the PDR position by about two orders of magnitude when taking these processes into account and advanced alternative explanations that (i) either CH₃CN originates from deeper inside of the cloud than previously assumed; or, (ii) the photo-desorption rate is higher and ice photolysis rate lower than those currently implemented in models; or, (iii) critical chemical formation pathways are missing in current astrochemical networks.

Another possible explanation for these high nitrile abundances could be the elemental gas-phase C/O ratio. Indeed, the relative elemental gas-phase abundances of oxygen and carbon are known to strongly impact the chemistry of star-forming regions (van Dishoeck & Blake 1998). For instance, small hydrocarbons, such as C₂H, C₃H, C₃H₂ and C₄H, observed in a wide variety of astrophysical objects including PDRs (Fuente et al. 2003; Pety et al. 2005, 2012; Cuadrado et al. 2015; Guzmán et al. 2015) and protoplanetary disks (Dutrey et al. 1997; Fuente et al. 2010; Henning et al. 2010; Qi et al. 2013; Kastner et al. 2015; Guilloteau et al. 2016; Bergin et al. 2016; Kastner et al. 2018; Cleeves et al. 2018; Bergner et al. 2019; Loomis et al. 2019), are believed to be mainly formed from atomic carbon (i.e. C⁺ and/or C). However, atomic carbon is readily converted into CO. Therefore, depending upon the UV-shielding and C/O ratio, more or less carbon can be locked into CO, hampering the production of hydrocarbons and more complex

carbon-containing molecules such as CH₃CN and HC₃N. In planet-forming disks, a super-solar C/O ratio ($\gtrsim 0.8$) explains the hydrocarbon observations well and is reasonably justified by oxygen removal through water formation and other non-volatile O-bearing species (e.g. Hogerheijde et al. 2011; Cleeves et al. 2018).

Here, we explore whether the observed CH₃CN and other complex nitriles in the Horsehead PDR can be explained by pure gas-phase chemistry when taking into account a revised understanding of the cosmic-ray (CR) ionization rate, a more complex gas-phase chemistry network, and most importantly, a C-rich environment. We then carry out a smaller study of complex nitrile production in planet-forming disks with elevated C/O ratios. In § 2, we describe the physical and chemical properties we used and developed within the Meudon PDR Code as well as our fiducial protoplanetary disk model. The resulting molecular abundances and their dependence upon the CR ionization rate, C/O ratio, and complex nitrile formation pathways are presented in § 3. In § 4, we discuss the dominant reaction pathways for the four nitrile molecules detected toward the Horsehead nebula - C₃N, HC₃N, CH₃CN and CH₃NC - as well as which parameters affect these nitrile abundances. Our conclusions are summarized in § 5.

2. MODELING

For the PDR chemical investigations we use the Meudon PDR Code, tuned to the physical conditions of the Horsehead nebula, and extended to incorporate a more complete gas-phase chemical network for nitriles up to CH₃CN and CH₃NC in complexity. In the second, smaller part of this paper we use a fiducial protoplanetary disk model previously described in Le Gal et al. (2019) to test whether our nitrile-optimized PDR chemistry can also explain high abundance of complex nitriles in disks.

2.1. PDR Physical structure

The Meudon PDR Code is a 1D astrochemical modeling code which considers a stationary plane-parallel slab of gas and dust illuminated by a radiation field (Le Petit et al. 2006), which can be introduced at will. Assuming a cloud at steady-state, it solves the physical and chemical conditions at different visual extinction throughout the cloud, taking into account radiative transfer from UV absorption, cooling emissions, and heating processes.

Figure 1 displays the typical physical structure we computed for the present study, assuming that the cloud has a fixed pressure of 4×10^6 K cm⁻³ in the PDR region, and a constant density of 2×10^5 cm⁻³ in the core (Habart et al. 2005), i.e. in our model for $A_V \gtrsim 2$ mag.

¹ <http://www.iram-institute.org/~horsehead/Horsehead.Nebula/WHISPER.html>

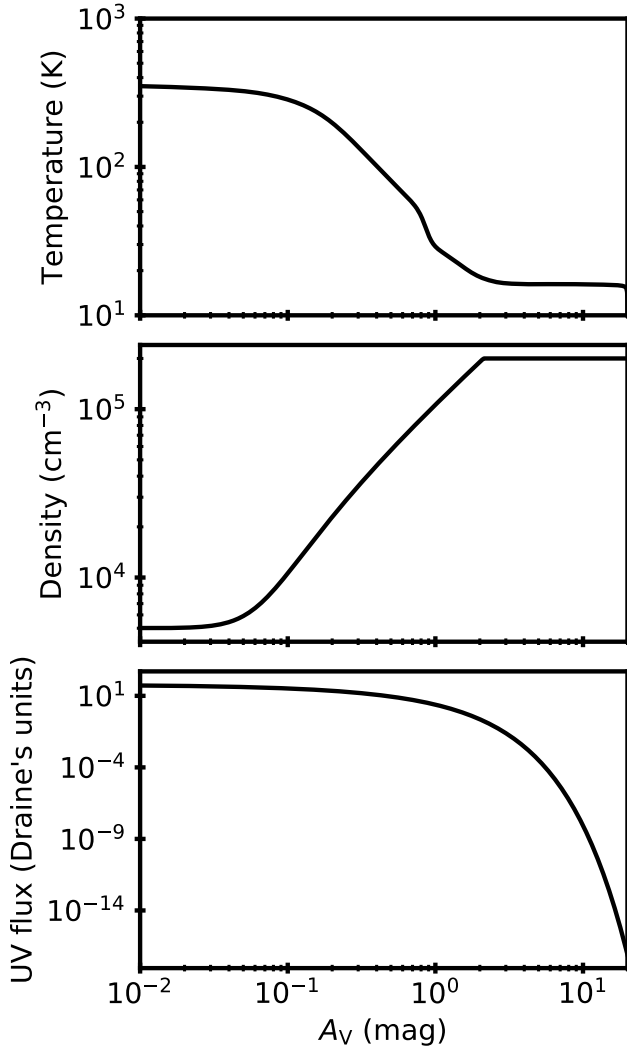


Figure 1. Horsehead nebula profiles of the temperature (top panel), the density (middle panel) and the UV flux (bottom panel) as function of the visual extinction, A_V .

The incident radiation upon this cloud is that of σ Ori, an O 9.5 V star system, which results in an incident FUV intensity upon the cloud of about $\chi = 60$ (i.e. $60 \times$ the ISRF in Draine’s units $\approx 60 \times 2.7 \times 10^{-3}$ erg s $^{-1}$ cm $^{-2}$, Draine 1978; Habart et al. 2005). The physical structure shown here was built considering standard initial gas-phase elemental abundances, see Table 1, i.e. a C/O ratio of ≈ 0.46 (Pety et al. 2005; Goicoechea et al. 2006).

Another parameter to consider is the CR ionization rate ζ . Low energy cosmic rays (10-100 MeV, e.g. Grenier et al. 2015) can penetrate deep into dense clouds, producing ions that drive the gas-phase chemistry via fast ion-neutral reactions. Diffuse clouds usually present higher values of ζ than denser clouds (e.g. Indriolo et al. 2015; Le Petit et al. 2016), with $\zeta \approx (1-5) \times 10^{-17}$ s $^{-1}$

Table 1. Initial gas-phase elemental abundances

Species	n_i/n_H ^(a)
He	0.1
O ^(b)	3.02×10^{-4}
C	1.38×10^{-4}
N	7.95×10^{-5}
S	3.50×10^{-6}
Si	1.73×10^{-8}
Fe	1.70×10^{-9}

NOTE—(a) from Pety et al. (2005) & Goicoechea et al. (2006) (b) To test the impact of the C/O ratio, we varied the oxygen elemental abundance in the range $[3.45 - 0.92] \times 10^{-4}$ (see § 3.2).

per H $_2$ being a typical dense cloud value (e.g. Goicoechea et al. 2009). We highlight here that what we labeled as ζ in the present study is the CR ionization rate per H $_2$, which corresponds to approximately twice the value of the CR ionization rate per H atom (Glassgold & Langer 1974). In a previous modeling study of the Horsehead nebula, Rimmer et al. (2012) found that chemical predictions are in better agreement with observations when ζ is allowed to vary across the cloud, considering the following equation adapted from Nath & Biermann (1994) by Rimmer et al. (2012):

$$\zeta = 3.05 \times 10^{-16} (A_V)^{-0.6} + 10^{-17} \text{ s}^{-1} \text{ per H}_2. \quad (1)$$

For the PDR position, where $A_V \approx 2$ mag, Eq. (1) gives $\zeta \approx 2 \times 10^{-16}$ s $^{-1}$ per H $_2$. In § 3, we test the impact of this higher value of ζ on the nitrile chemistry, by comparison to the canonical value of $\zeta = 5 \times 10^{-17}$ s $^{-1}$ per H $_2$ used in Pety et al. (2005) and Goicoechea et al. (2006).

Lastly, while the public version of the Meudon PDR Code (v.1.5.2) does not include grain chemistry, it does model the formation of H $_2$ on grains and computes the charge and temperature distribution of grains. In this study, we kept the default grain size distribution, i.e. with grain radius from 1×10^{-3} to $0.3 \mu\text{m}$ and their relative abundances described by the MRN distribution (Mathis et al. 1977).

2.2. PDR model Chemistry

Each model was performed using the same initial abundance set as in Pety et al. (2005) and Goicoechea et al. (2006), except for the oxygen abundance that we varied in some models to explore the impact of the C/O ratio on the chemistry (Table 1). We updated and extended the PDR Meudon Code (v.1.5.2) chemi-

cal network with 39 species and 913 reactions relevant to the chemistry of C_3N , HC_3N , and CH_3CN , that we extracted from the KIDA database² for most of them. We also extended the chemical network to the chemistry of CH_3NC , based on theoretical studies (e.g. [Defrees et al. 1985](#)) and the chemistry of its isomer CH_3CN (see § 3.3). In total, our network is composed of 191 species and 3616 chemical reactions, including gas-phase bi-molecular reactions (i.e. radiative associations, ion-neutral and neutral-neutral reactions), recombinations with electrons, ionization and dissociation reactions by direct cosmic rays and secondary photons (i.e. photons induced by cosmic rays), and by UV-photons (see [Le Petit et al. 2006](#), for rate formulae details). The critical reactions discussed in this paper are summarized in [Table A1](#), with rates and references.

UV-photo-reactions are expected to play a crucial role in PDR chemistry. The `Meudon PDR Code` allows the choice between two different methods to compute the photo-reaction rates: 1) if the photo-ionization and/or photo-dissociation cross-sections of the molecule is known, the most accurate approach consists in integrating this cross-section over the radiation field at each given position in the cloud; 2) if the photo-cross-section of the molecule is unknown, an analytical expression as function of the visual extinction is estimated, i.e. considering fixed fitted parameters for each molecules and computing their photo-rates as function of the visual extinction (see for an example Eq. (14) of [Heays et al. 2017](#)). We updated the cross-sections of all the molecules available in the Leiden database³ that are included in our chemical network in the `Meudon PDR Code` ([Heays et al. 2017](#)).

2.3. Protoplanetary disk physical structure

Our fiducial protoplanetary disk astrochemical model is based on the MWC 480 disk model of [Le Gal et al. \(2019\)](#), which consists in a 2D parametric physical structure onto which the chemistry is post-processed (see §2.4). The disk physical structure assumes a disk that is symmetric azimuthally and with respect to the midplane. Thus, it can be described in cylindrical coordinates centered on the inner star along two perpendicular axes characterizing the radius and height in the disk. [Figure 2](#) represents the profiles of the gas temperature, density, visual extinction and UV flux throughout the disk, for which the parameterization is briefly summarized below and further described in [Le Gal et al. \(2019\)](#).

For a given radius r from the central star, the vertical temperature profile is computed following the formalism of [Rosenfeld et al. \(2013\)](#) and [Williams & Best \(2014\)](#), originally developed by [Dartois et al. \(2003\)](#):

$$T(z) = \begin{cases} T_{\text{mid}} + (T_{\text{atm}} - T_{\text{mid}}) \left[\sin\left(\frac{\pi z}{2z_q}\right) \right]^{2\delta} & \text{if } z < z_q \\ T_{\text{atm}} & \text{if } z \geq z_q, \end{cases} \quad (2)$$

where T_{mid} and T_{atm} are respectively the midplane and atmosphere temperatures that vary as power law of the radii ([Beckwith et al. 1990](#); [Piétu et al. 2007](#); [Le Gal et al. 2019](#)). $z_q = 4H$ with H the pressure scale height that, assuming vertical static equilibrium, can be expressed as follows:

$$H = \sqrt{\frac{k_B T_{\text{mid}} r^3}{\mu m_H G M_\star}}, \quad (3)$$

with k_B the Boltzmann constant, $\mu = 2.4$ the reduced mass of the gas, m_H the proton mass, G the gravitational constant, and M_\star the mass of the central star. The midplane temperature T_{mid} is estimated following a simple irradiated passive flared disk approximation (e.g. [Chiang & Goldreich 1997](#); [Dullemond et al. 2001](#); [Huang et al. 2018](#)):

$$T_{\text{mid}}(r) \approx \left(\frac{\varphi L_\star}{8\pi r^2 \sigma_{\text{SB}}} \right)^{1/4}, \quad (4)$$

with $L_\star = 24 L_\odot$ the stellar luminosity ([Andrews et al. 2013](#)), σ_{SB} the Stefan-Boltzman constant and $\varphi = 0.05$ a typical flaring angle. The atmosphere temperature, T_{atm} , is based on observational constraints. So here we consider $T_{\text{atm}} = T_{\text{atm},100 \text{ au}} \left(\frac{r}{100 \text{ au}} \right)$, with $T_{\text{atm},100 \text{ au}} = 48 \text{ K}$ from [Guilloteau et al. \(2011\)](#).

The disk is assumed to be in hydrostatic equilibrium. Thus, for a given vertical temperature profile, the vertical density structure is determined by solving the equation of hydrostatic equilibrium, as described from Eq. (17) to (20) in [Le Gal et al. \(2019\)](#). The surface density of the disk is assumed to follow a simple power law varying as $r^{-3/2}$ ([Shakura & Sunyaev 1973](#); [Hersant et al. 2009](#)):

$$\Sigma(r) = \Sigma_{R_c} \left(\frac{r}{R_c} \right)^{-3/2}, \quad (5)$$

where Σ_{R_c} is the surface density at the characteristic radius that can be expressed as function of the mass of the disk, M_{disk} , and its outer radius, R_{out} :

$$\Sigma_{R_c} = \frac{M_{\text{disk}} R_c^{-3/2}}{4\pi \sqrt{R_{\text{out}}}}, \quad (6)$$

with here $M_{\text{disk}} = 0.18 M_\odot$ ([Guilloteau et al. 2011](#)).

² <http://kida.obs.u-bordeaux1.fr/>

³ <https://home.strw.leidenuniv.nl/~ewine/photo/>

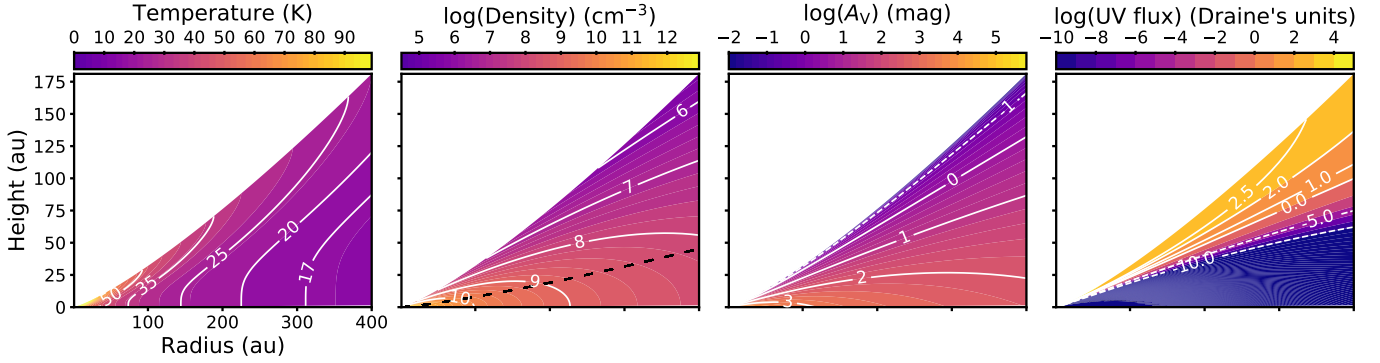


Figure 2. Disk physical structure fed in our fiducial protoplanetary disk astrochemical model. The 2D temperature (*first panel*), density (*second panel*), visual extinction (*third panel*) and UV flux (*fourth panel*) profiles are represented as functions of disk radius versus height, both in au. The dashed black line, on the densities panels, delineates 1 scale height.

The visual extinction profile is derived from the hydrostatic density profile using the gas-to-extinction ratio of $N_{\text{H}}/A_{\text{V}} = 1.6 \times 10^{21}$ (Wagenblast & Hartquist 1989), with $N_{\text{H}} = N(\text{H}) + 2N(\text{H}_2)$ the vertical hydrogen column density of hydrogen nuclei. This gas-to-extinction ratio assumes a typical mean grain radius size of $0.1 \mu\text{m}$ and dust-to-mass ratio of 0.01, consistent with model assumptions.

Finally, the UV flux profile is computed considering the UV flux impinging the disk convolved with the visual extinction profile. The unattenuated UV flux factor, f_{UV} , at a given radius r depends on both the photons coming directly from the central embedded star and on the photons that are downward-scattered by small grains in the upper atmosphere of the disk. Thus, following Wakelam et al. (2016), we consider:

$$f_{\text{UV}} = \frac{f_{\text{UV}, R_c}/2}{\left(\frac{r}{R_c}\right)^2 + \left(\frac{4\text{H}}{R_c}\right)^2}. \quad (7)$$

2.4. Protoplanetary disk chemical model

The disk chemistry is computed time-dependently in 1+1D using the gas-grain astrochemical model *Nautilus* (v.1.1) (Hersant et al. 2009; Wakelam et al. 2016) in three phase mode (Ruaud et al. 2016), i.e. including gas-phase, grain-surface and grain-bulk chemistry (see Le Gal et al. 2019, for more details). First, the chemical evolution of a representative starless dense molecular cloud is modeled up to a characteristic age of 1×10^6 years (e.g. Elmegreen 2000; Hartmann et al. 2001). For this 0D model we use typical constant physical conditions: grain and gas temperatures of 10 K, a gas density of $2 \times 10^4 \text{ cm}^{-3}$ and $\zeta = 5 \times 10^{-17} \text{ s}^{-1}$ per H_2 ; this parent molecular cloud is also considered to be shielded from external UV photons by a visual extinction of 30 mag. For consistency, we use the same initial abundances as for our PDR model (see Table 1) for this first simulation step. The outcoming chemical gas and

ice compositions of this parent molecular cloud are then used as initial chemistry for our 1+1D disk model. Second, we ran the chemistry of our 1+1D disk model up to one million years, typical chemical age of a disk when grain growth is not considered (e.g. Cleaves et al. 2015). While the disk chemistry has not reached steady state at that time, its evolution is slow enough that the results presented here hold for a disk twice younger or older. Note that in contrast to the PDR model, the disk chemical code does include grain surface reactions. However the grain-surface reactions pathways to CH_3CN and HC_3N , the two molecules of particular interest for this study, remain poorly constrained.

3. RESULTS

3.1. Impact of cosmic-ray treatment

Figure 3 presents the abundances of C_3N , HC_3N and CH_3CN computed with the Meudon PDR Code as function of the visual extinction A_{V} , for two models. Both models consider our new chemical network and the initial gas-phase elemental abundances prescribed in Pety et al. (2005) and Goicoechea et al. (2006) (see Table 1) but each model uses a different CR ionization rate. The *standard* model uses the CR ionization rate canonical value of $\zeta = 5 \times 10^{-17} \text{ s}^{-1}$ per H_2 (Pety et al. 2005; Goicoechea et al. 2006), and the *high- ζ* model uses a higher CR ionization rate of $\zeta = 2 \times 10^{-16} \text{ s}^{-1}$ per H_2 , as calculated from (Eq. 1). By impacting the ion abundances in molecular clouds, the CR ionization rate indirectly drives the abundances of their daughter neutral molecules (see § 2.1). The nitrile abundances are indeed higher with the *high- ζ* model than with the *standard* model, but both models under-predict by several orders of magnitude the abundances observed toward the Horsehead nebula.

Rimmer et al. (2012) showed that a varying ζ across the cloud tends to produce more accurate results. How-

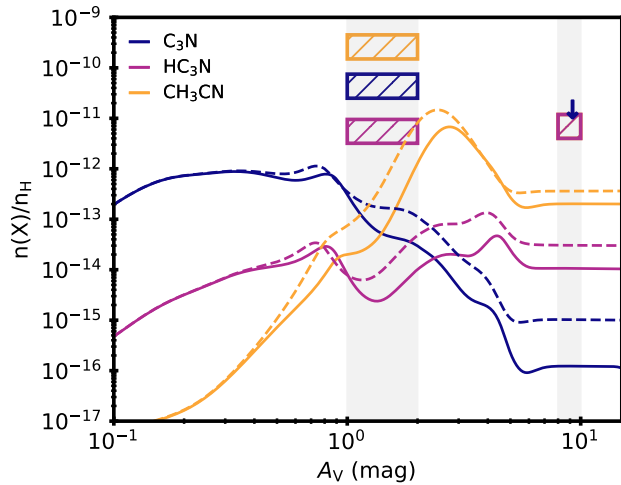


Figure 3. Computed C_3N (dark blue) HC_3N (purple) and CH_3CN (orange) abundances with respect to H nuclei, as function of the visual extinction A_V obtained with the *standard* model (solid lines) and with the *high- ζ* model (dashed lines), see § 3.1. These model results are compared to the observations from Gratier et al. (2013) (dashed boxes and arrow). 50% error bars are included on the observations. The PDR ($1 \text{ mag} < A_V < 2 \text{ mag}$) and Core ($A_V \gtrsim 8 \text{ mag}$) regions are shaded.

ever, for the visual extinctions associated with the PDR region and for molecules of interest studied here, varying ζ across the cloud does not significantly impact the results compared to a constant- ζ model. In the Core region, the varying-versus-constant ζ model abundances are about half an order of magnitude different.

Changing the CR ionization rate also impacts the gas temperature, as shown in the bottom panels of Fig. 4. Typically, increasing ζ shifts the temperature gradient closer to the PDR’s edge. As a result, a higher ζ leading to higher temperatures and thus higher reaction rates, the absolute abundances of nitriles are slightly increased in the PDR with a *high- ζ* model. In addition, likely due to the shift in temperature, the abundance patterns are shifted outwards (i.e. closer to the illuminated edge of the PDR) in the case of a higher ζ . In summary, while the CR treatment has an impact on the complex nitrile chemistry, increasing nitrile abundances by almost an order of magnitude in the PDR region, the effect is small compared to the mismatch between models and observations (see Fig. 3).

3.2. Impact of the C/O ratio

Major carriers of O and C are expected to freeze out under different conditions. In particular a substantial amount of O can become incorporated into water ice which is one of the least volatile common interstellar molecules, resulting in an elevated C/O ratio in the gas-

phase. In order to mimic the differential freeze-out of volatiles on grains, we varied the oxygen gas-phase elemental abundance from 3.45×10^{-4} to 9.2×10^{-5} while keeping the carbon abundance fixed. This led to a variation of the C/O ratio from 0.4 to 1.5. The lowest considered O abundance is a factor of two higher than the CO abundance derived in the Horsehead PDR (5.6×10^{-5} , Pety et al. 2005), while the highest considered O abundances is below the cosmic O abundance of 4.9×10^{-4} (Asplund et al. 2009) to 5.75×10^{-4} (Przybilla et al. 2008). The choice of fixing the carbon elemental abundance and varying the oxygen one, is also justified by the fact that, between these two elements, the elemental gas-phase abundance of oxygen is the less constrained (Jenkins 2009; Whittet 2010; Jones & Ysrad 2019), as discussed in Le Gal et al. (2014).

Figure 4 shows the impact of the gas-phase C/O ratio on the abundances of C_3N , HC_3N and CH_3CN and on the gas temperature as function of the visual extinction A_V in our model of the Horsehead nebula. An O-poor chemistry (i.e. a high C/O ratio) results in higher abundances of the three nitriles. For a CR ionization rate of $\zeta = 2 \times 10^{-16} \text{ s}^{-1}$ per H_2 and a gas-phase C/O ratio in the range 0.9 – 1.5, our new gas-phase chemistry model can reproduce the three nitrile observations at the PDR position within an order of magnitude. As for the Core position, our best fit models are found for lower C/O ratios, in the range 0.6 – 0.9. This lowering of C/O with increasing visual extinction could be explained by photon-mediated release of refractory carbon into gas phase in the PDR region, and/or the onset of freeze out of carbon species in the core region. Whatever the mechanism, the decrease of C/O with increasing visual extinction suggests that the gas-phase C/O ratio vary across astrophysical objects.

It is also important to mention that the chemical rates used in astrochemical models sometimes present large uncertainties. We ran two additional models to test the impact of such uncertainties on the major reaction rates listed in Table A1 which are driving the complex nitrile chemistry. These additional simulations compute the chemistry with (i) the maximum allowed rates, and (ii) the minimum allowed rates. The results are that the nitrile abundances of interest for this study vary by less than a factor of three in the PDR and Core regions, which is small compared to the more than two orders of magnitude mismatch between observations and models using the standard C/O value. Though this does not constitute a rigorous detailed sensitivity analysis such as those developed for instance by Vasyunin et al. (2004, 2008) and Wakelam et al. (2005, 2006, 2010), our simple analysis suggests that our results are robust.

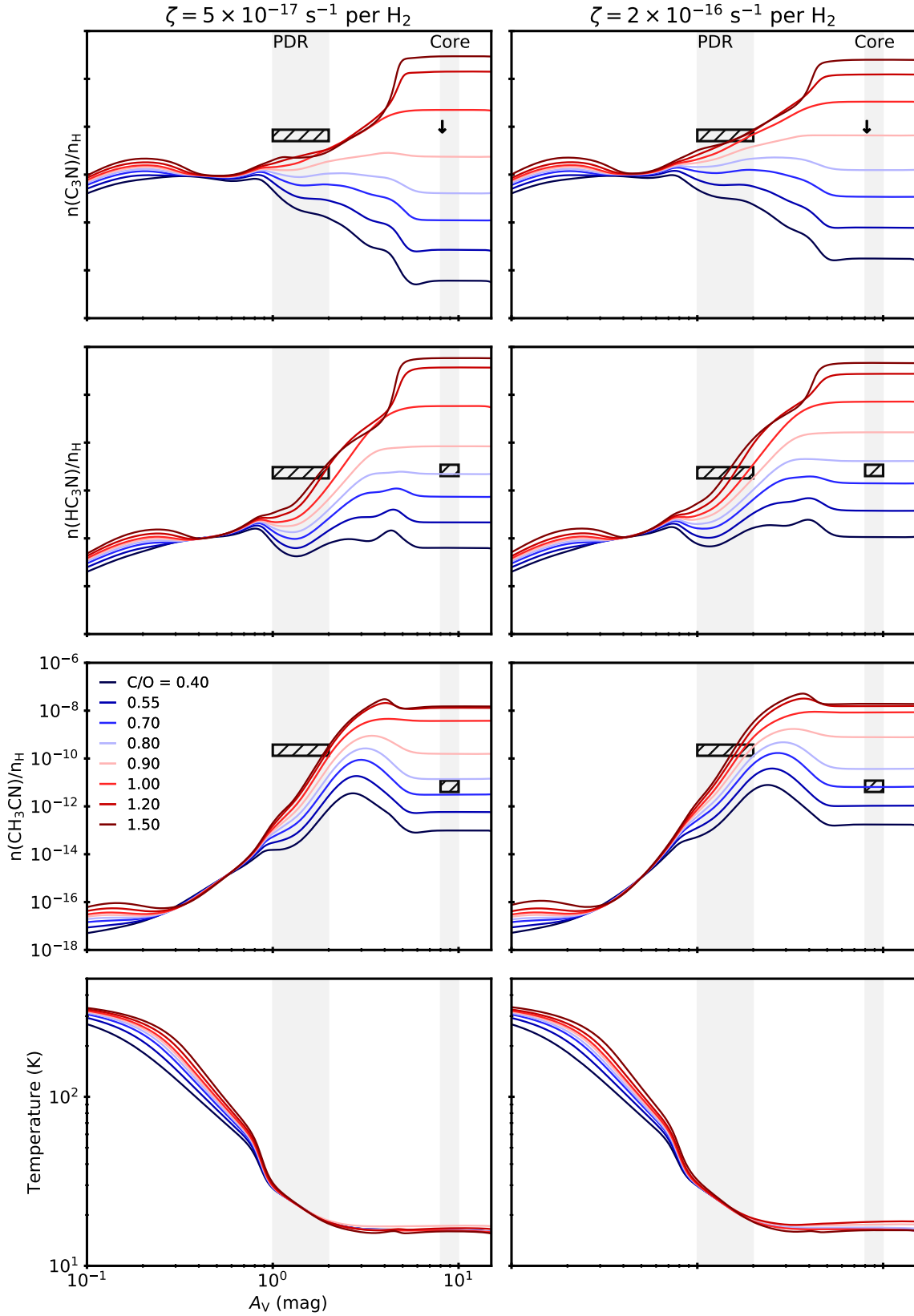


Figure 4. C_3N , HC_3N and CH_3CN abundances with respect to H nuclei, as well as the gas temperature, computed with our model of the Horsehead nebula as function of the visual extinction, A_V , for varying C/O and the standard- (left column) and high- (right column) CR ionization rates considered in this study. The observations from Gratier et al. (2013) are represented by the black hatched boxes, which consider 50% error bars, and the downward arrow. The core ($A_V > 8$ mag) and PDR ($1 \text{ mag} < A_V < 2$ mag) regions are shaded.

Since we are mainly interested in the PDR nitrile chemistry, we consider our best-fit model the model with the lowest C/O ratio that reproduces at the PDR position the three complex nitrile abundances shown Fig. 4. The model with $\zeta = 2 \times 10^{-16} \text{ s}^{-1}$ per H_2 and $\text{C/O} = 1.0$ fulfills these criteria.

Figure 5 shows the modeled abundances, obtained with our best-fit model, of other typical oxygenated and carbonated molecules that were also observed toward the Horsehead nebula, i.e. CO (Pety et al. 2005), HCO^+ (Goicoechea et al. 2009), H_2CO (Guzmán et al. 2011), and the hydrocarbons C_2H , $c\text{-C}_3\text{H}$, and C_4H (Pety et al. 2005; Guzmán et al. 2015). For comparison, the *standard* model results are also presented in the same figure. The C/O variation does not significantly impact the CO abundance throughout the cloud, which is consistent with the fact that CO is the main reservoir of carbon and the carbon elemental abundance is fixed in our models. Our best fit model displays better agreement between model and observations in the PDR for the other O-bearing molecules we consider, H_2CO and HCO^+ .

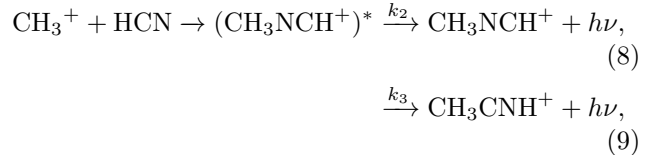
With regards to the hydrocarbons, our best model better matches the observations at the PDR position, generally by orders of magnitude, compared to the standard model. This is an expected result because atomic O is a main destroyer for small hydrocarbons such as C_2H , $c\text{-C}_3\text{H}$ and C_4H (Millar et al. 1987; Millar & Herbst 1990). Thus, while C is kept constant, diminishing O increases the hydrocarbon abundances. However, even our best fit model does not fully reproduce the observed abundances (see for instance C_4H in Fig. 5), indicative of that the C/O ratio does not provide a complete explanation for the abundant hydrocarbon chemistry in the Horsehead PDR.

Regarding the Core position, our best fit model generally over-predicts the observations, but this might simply be explained by the fact that freeze-out on grains is not included in our model. It could also be that the gas-phase C/O ratio decreases within the nebula, as suggested by the C/O grid results shown in Fig. 4 when compared to the observations in each observed positions.

3.3. CH_3NC vs CH_3CN chemical pathways

Another interesting nitrile molecule to study is the methyl isocyanide (CH_3NC), the isomer of methyl cyanide (CH_3CN). First detected toward Sgr B2 (Cernicharo et al. 1988; Remijan et al. 2005), CH_3NC was also detected toward the Horsehead nebula (Gratier et al. 2013), Orion KL (López et al. 2014), and more recently toward the solar-type binary protostar IRAS 16293-2422 (Calcutt et al. 2018). A few theo-

retical and experimental studies have investigated the isomers' chemistry and their abundance ratio (Huntress & Mitchell 1979; Defrees et al. 1985; Anicich et al. 1995), and converged on the same major gas-phase production pathways for both via the reaction:



with k_2 and k_3 given in Table A1, followed by the dissociative recombinations of both protonated ions CH_3NCH^+ and its isomer CH_3CNH^+ to form CH_3NC and CH_3CN , respectively (see reaction rates in Table A1). However, the branching ratio is poorly constrained and depends on the stabilization processes of the intermediate complex $(\text{CH}_3\text{NCH}^+)^*$ (e.g. Anicich et al. 1995). Due to its lower energy state, CH_3CNH^+ is found to be the major product of the reaction $\text{CH}_3^+ + \text{HCN}$ (9). However, its formation requires the isomerization of the intermediate complex $(\text{CH}_3\text{NCH}^+)^*$, which likely happens due to collisions with a third body. Thus, the ratio between the two isomeric ions depends on the competition between the relaxation and isomerization rates of the intermediary complex. The resulting $\text{CH}_3\text{NCH}^+/\text{CH}_3\text{CNH}^+$ ratio was estimated to lie in the range 0.1–0.4 by one theoretical study and assumed to propagate to a $\text{CH}_3\text{NC}/\text{CH}_3\text{CN}$ ratio of 0.1–0.4 via the respective subsequent dissociative recombinations (Defrees et al. 1985).

Here, we investigated the impact of the branching ratios in between the pathways (8) and (9) on the resulting $\text{CH}_3\text{NC}/\text{CH}_3\text{CN}$ ratio in our PDR model. Figure 6 presents the results obtained using our best fit model and three different branching ratios leading to: 100%, 80% and 0% of isomerization. The best fit results are obtained for a branching ratio of 80% (i.e. $\text{CH}_3\text{NC}/\text{CH}_3\text{CN} \sim 0.2$), in agreement with the theoretical calculation of Defrees et al. (1985). However, to our knowledge the CH_3NCH^+ dissociative recombination has not been studied yet and even though the rate of the CH_3CND^+ dissociative recombination was measured (Vigen et al. 2008) its branching ratio remains uncertain (e.g. Plessis et al. 2010, 2012; Loison et al. 2014). It would thus be interesting to study whether the dissociative recombination of CH_3CNH^+ and CH_3NCH^+ could lead to disproportionate prevalence of each initial isomer. Further theoretical and experimental studies are therefore needed to assess the validity of our astrochemically motivated branching ratios.

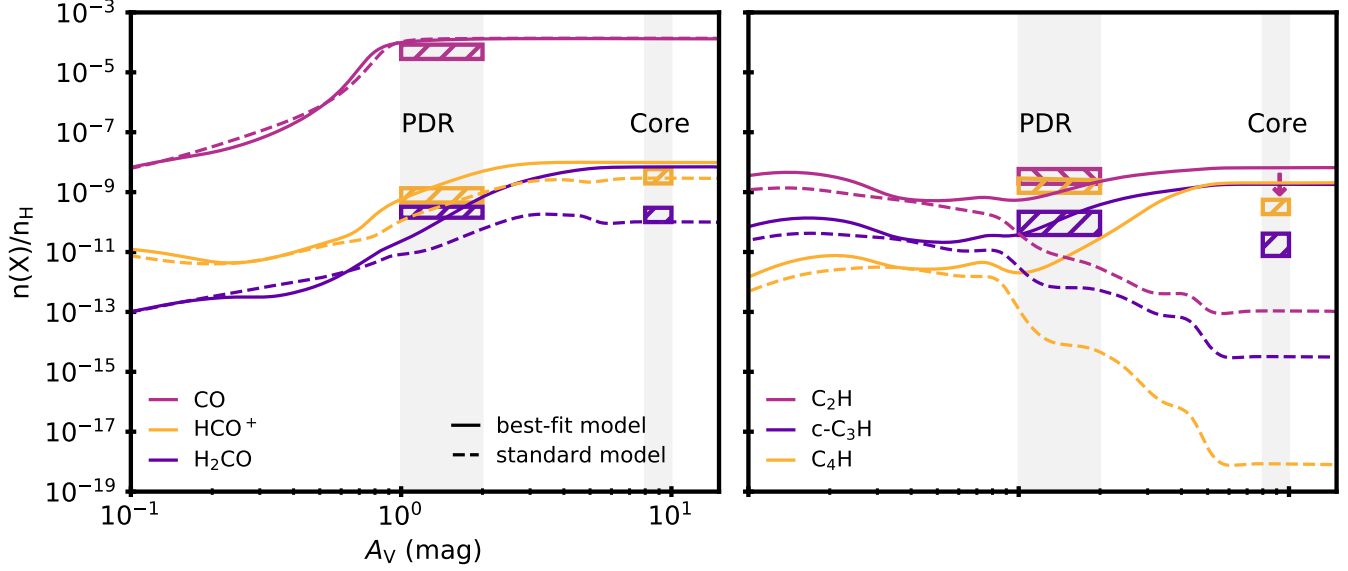


Figure 5. CO, HCO⁺, H₂CO, C₂H, c-C₃H and C₄H abundances with respect to H nuclei, as function of the visual extinction A_V computed with our best-fit model (solid lines) and standard model (dashed lines) of the Horsehead nebula, compared to published observations (Pety et al. 2005; Goicoechea et al. 2009; Guzmán et al. 2011, 2015) represented by the filled and hatched boxes and the downward arrows. 50% error bars are included on the observations. The core ($A_V > 8$ mag) and PDR ($1 \text{ mag} < A_V < 2 \text{ mag}$) regions are shaded.

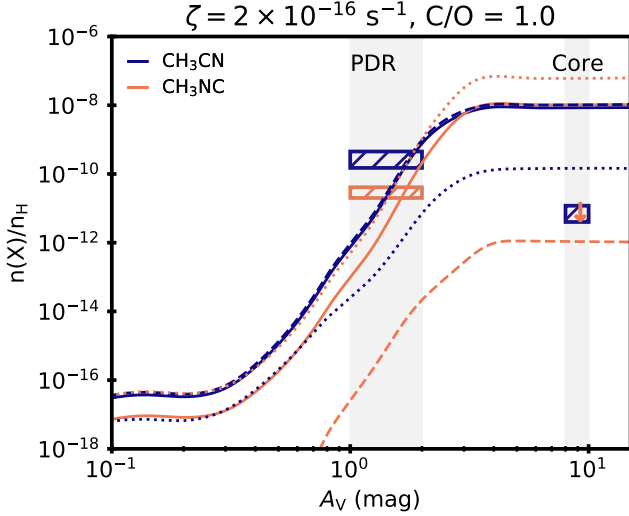


Figure 6. CH₃CN (dark blue) and CH₃NC (orange) abundances with respect to H nuclei, as function of the visual extinction, A_V , in the modeled Horsehead nebula. Three different models, based on our best-fit model (see § 3.2), are depicted here, testing the isomerization branching ratio of the reaction pathway (9): (i) 100% (dotted lines); (ii) 80% (solid lines - best model); (iii) 0% (dashed lines). The model results are also compared to published observations from Gratier et al. (2013), where 50% error bars are included (dashed boxes and downward arrow). The core ($A_V > 8$ mag) and PDR ($1 \text{ mag} < A_V < 2 \text{ mag}$) regions are shaded.

3.4. Complex nitrile production in a protoplanetary disk with a high C/O ratio

To test if our new understanding of the complex nitrile PDR chemistry can be generalized to disks, we used a fiducial protoplanetary disk astrochemical model, loosely based on the disk around MWC 480, from Le Gal et al. (2019) described § 2.3 and § 2.4. We ran the chemical post-processing for two different C/O ratios: (i) C/O= 0.46, as in our PDR *standard* model, and (ii) C/O= 1.0 as in our PDR best fit model. For each of these C/O ratios we ran two disk models, a full gas-grain model and a gas-grain model where CH₃CN and HC₃N are only formed in the gas phase. The results of this total of four disk models on the abundances of HC₃N and CH₃CN are shown in Fig. 7. A huge gap is observed from ~ 25 to ~ 200 au in the computed nitrile column densities for the standard C/O ratio disk models, and disappears for higher C/O. The prevalence of grains' pathway formation increases with C/O, and even becomes negligible in the formation of HC₃N for standard C/O. Even though our disk model also includes grain chemistry, the main result from our PDR study holds for disk astrochemistry, i.e. that an elevated C/O ratio better reproduce the nitrile observations. Without any tuning of our disk model, our best-fit model predictions are within an order of magnitude for the CH₃CN case. For the HC₃N, the results are in agreement, at the order of magnitude level, for the inner 100 au of

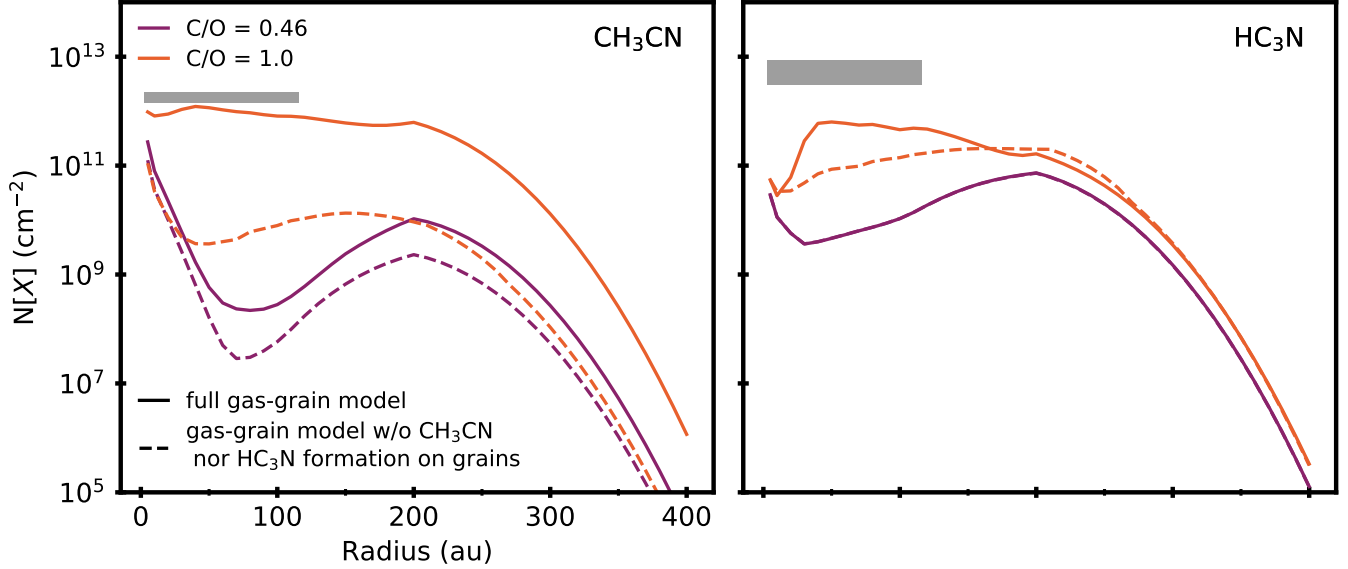


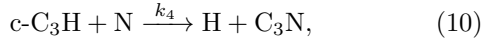
Figure 7. Radial profile of the column density of CH_3CN and HC_3N computed with our fiducial protoplanetary disk astrochemical model for four different models, differing in (i) their C/O ratio, with (a) C/O= 0.46 (in purple) as in our PDR *standard* model and (b) C/O= 1.0 (in orange) as in our PDR best fit model; (ii) their grain chemical network that includes (solid lines) or not (dashes lines) the formation of CH_3CN and HC_3N on grains. The horizontal gray lines represent the column density derived from the MWC 480 disk observations of (Bergner et al. 2018).

the disk, where likely most of the emission originates (Bergner et al. 2018).

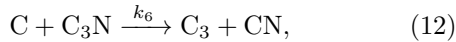
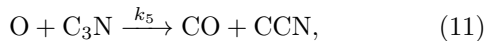
4. DISCUSSION

4.1. Nitrile formation pathways

In our PDR models, the C_3N formation is dominated by the reaction:



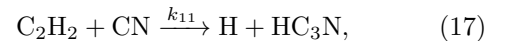
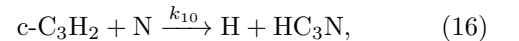
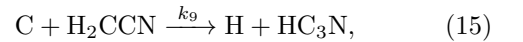
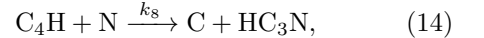
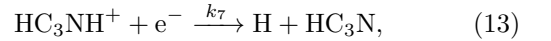
with k_4 given in Table A1. $\text{c-C}_3\text{H}$ being itself mainly produced by the electronic recombination of $\text{c-C}_3\text{H}_2^+$. Thus, the under-prediction of C_3N by our model in the PDR region could be explained by the under-prediction of $\text{c-C}_3\text{H}$ (see Fig. 5). Therefore, for a fixed abundance of N, a carbon-enriched medium would enhance the production of C_3N . As for its destruction, photo-dissociation dominates in the PDR (see the corresponding reaction rate Table A1), but depending on the C/O ratio two other reactions also participate in the C_3N destruction, i.e.:



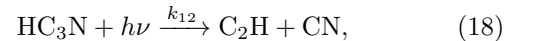
with k_5 and k_6 given in Table A1. Reaction (11) even becomes the primary destruction pathway of C_3N in O-rich (C/O \approx 0.4) PDR. While, a priori, it may seem

odd for a photo-dissociation process to not be the primary destruction mechanism in PDR, in our model this is explained by the high concentration of atomic oxygen in this region for low C/O ratios. In O-poor (C/O \gtrsim 1) PDR, C_3N is primarily destroyed through a combination of photo-dissociation and by atomic carbon (12).

HC_3N is formed from a variety of different reactions involving carbon- and nitrogen-containing molecules:



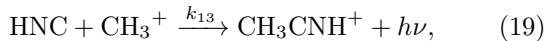
with k_7 to k_{11} given in Table A1. Thus, with a lower amount of one of the main hydrocarbon destroyer, atomic O, and a higher amount of ‘free’ carbon in the gas phase, more reaction pathways meaningfully contribute to the formation of HC_3N , via these diverse carbon-rich intermediates. HC_3N is mainly destroyed by UV-photons up to an $A_V \approx 4$ mag, via the reaction:



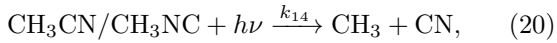
with k_{12} given in Table A1. For $A_V \gtrsim 4$ mag, the impact of destruction by dominant ions (e.g. H^+ , H_3^+ ,

H_3O^+ , C^+ , HCO^+) gradually increases with the optical depth, since UV-photon penetration diminishes and most of the ion abundances increase. Other destruction pathways involving atomic carbon forming bigger carbon chain molecules appear with increasing optical depth, but these are typically far less common in our grid models and are only relevant in dense clouds with higher carbon abundances.

The formation of CH_3CN is dominated by the dissociative recombination of CH_3CNH^+ with electrons, where CH_3CNH^+ itself is primarily formed by the radiative association (9) and the following:



with k_{13} given in Table A1. Similarly, and as already presented in § 3.3, the formation of CH_3NC is dominated by the dissociative recombination of CH_3NCH^+ with electrons, with CH_3NCH^+ primarily formed by the radiative association (8). CH_3^+ is formed via successive hydrogenation from C^+ . HCN and HNC also descend from atomic carbon (Le Gal et al. 2014; Loison et al. 2014). As a consequence, the formations of CH_3CN and its isomer CH_3NC seem to be guided mostly by the carbon abundance, explaining that the abundance of CH_3CN increases with C/O (see Fig. 4). The destruction of the isomers are dominated by photo-dissociation:



with k_{14} given in Table A1.

To summarize, the enhancement in nitrile abundances appear to be tightly correlated with the C/O ratio. More interestingly however, our study highlights the importance of the relative elemental gas-phase abundances with respect to one another, and emphasizes the indirect role of oxygen in nitrile chemistry. The latter has a dramatic impact on the carbon chemistry in O-rich molecular environments, where most of the carbon is rapidly locked in CO and atomic O is a main destroyer for hydrocarbons, hampering the development of more complex carbon chemistry. In addition, we have shown in § 3.2 that the nitrile abundances increase with ζ (Fig. 4). Indeed, the ionization fraction is directly linked to ζ , which governs the production of ions, such as CH_3^+ , HC_3NH^+ and $c\text{-C}_3\text{H}_2^+$, parent molecules of the complex nitriles here under study. CH_3^+ react with HCN and HNC to produce CH_3CNH^+ , that readily recombines with electrons to form CH_3CN ; HC_3NH^+ recombines with electrons to form HC_3N (13); and $c\text{-C}_3\text{H}_2^+$ recombines with electrons to form $c\text{-C}_3\text{H}$ which reacts with N to produce C_3N (10).

4.2. The role of C/O in PDR and disk atmosphere nitrile chemistry

The strong impact of the C/O ratio on the nitrile chemistry can likely be explained by the fact that in the gas phase, for a fixed amount of C element, O-removal decreases one of the main destruction pathways of hydrocarbons, which are the parent molecules of nitriles. To this effect adds the reactions of small carbon and oxygen species to form CO. Typically, in molecular clouds, most of the carbon hastily reacts with all available oxygen to form CO, effectively removing it from the reaction pathways that build up more complex molecules, such as complex nitriles. O-removal thus leaves more ‘free’ carbon available in the gas phase to form carbon-containing molecules such as hydrocarbons, carbon chains and nitriles. As a comparison, the *standard* model results in a CO abundance of almost 1.38×10^{-4} , i.e. quasi all the carbon available in our models (see Table 1), whereas our best-fit model produces a CO abundance of $\sim 1.34 \times 10^{-4}$. This leaves $\sim 6.0 \times 10^{-6}$ ‘free’ carbon to build more complex carbon-containing molecules.

Varying the C/O ratio also impacts the gas temperature for $A_V \lesssim 1.5$ mag, as shown in the last panel row of Fig. 4. An increase in C/O ratio increases the gas temperature. This is due to the fact that, in the present work, we varied the abundance of atomic O to change the C/O ratio, thus reducing one of the main gas coolant in this region of the PDR. To test the impact of varying the C/O ratio via the carbon elemental abundance instead of the oxygen, we ran additional models. The main difference is in the resulting CO abundance. For a fixed C/O ratio, it increases with the amount of carbon. As a consequence, the gas temperature decreases at the edge of the PDR, since CO is another important gas coolant. However, these differences diminish with the increase of the visual extinction and are minor at the PDR position and in particular on the nitrile abundances. Thus, the main results found in the present work on the C/O impact on the Horsehead nebula chemistry is agnostic to whether C or O is varied to achieve a C/O ratio of ~ 1 .

In disks, the C/O ratio is also strongly impacting the nitrile chemistry with the additional effect of changing the morphology of the nitrile abundance throughout the disk, as shown in Fig. 7. Whether or not CH_3CN forms in gas or through gas-grain chemistry in disks, an elevated C/O in disks also helps in better reproducing the observations. However, grain chemistry seems to be needed to better reproduce the observations, in agreement with Öberg et al. (2015) and Loomis et al. (2018). Our finding of a $\text{C/O} \gtrsim 1$ needed to reproduce the complex nitriles chemistry observed in disk atmospheres is in good agreement with the results of Bergin et al. (2016)

that also find that a C/O ratio exceeding unity is required to reproduce the observations of C₂H in disks. These authors therefore proposed C₂H as probe of C/O-enriched disk layers. Here we propose that complex nitriles could also serve as such probe in both PDR and disks, with the vantage of also probing the internal parts of the latter ($\lesssim 100$ au) as predicted by our models (see Fig. 7). Moreover, the fact that complex nitriles, such as HC₃N and CH₃CN, are much more commonly observed in disks than O-containing complex molecules, such as CH₃OH, highly suggests that organic chemistry is regulated by the C/O ratio and that disk atmosphere chemistry seems to be more generally C-rich than O-rich.

5. CONCLUSIONS

We tackled the chemistry of nitriles in PDR, in order to, first, understand the observations found for the nitriles C₃N, HC₃N, CH₃CN and CH₃NC toward the Horsehead PDR (Gratier et al. 2013), and second, test if our improved PDR chemistry could help to explain the recent observations of HC₃N and CH₃CN in disk atmospheres (Öberg et al. 2015; Bergner et al. 2018). To this aim, we extended the chemistry of the Meudon PDR code (v.1.5.2) up to these four nitriles and explored the impact of some key parameters, such as the cosmic-ray ionization rate ζ and the gas-phase elemental C/O ratio, on our modeled nitrile results. Our main conclusions are summarized below:

1. Varying the C/O ratio between 0.4 and 1.5 in a model of the Horsehead PDR results in orders of magnitude changes in nitrile abundances.
2. A gas-phase C/O ratio of $\gtrsim 0.9$ can reproduce the C₃N, HC₃N, CH₃CN and CH₃NC abundances within an order of magnitude in the Horsehead PDR, without any grain-surface chemistry.
3. The cosmic-ray ionization rate moderately affects the nitrile chemistry through its impact on electrons and hydrocarbon ions (e.g. CH₃⁺, C₃H₂⁺). A $\zeta = 2 \times 10^{-16} \text{ s}^{-1}$ per H₂ better fits the observations than the standard value of $\zeta = 5 \times 10^{-17} \text{ s}^{-1}$ per H₂.
4. Our best fit PDR model (i.e. with $\zeta = 2 \times 10^{-16} \text{ s}^{-1}$ per H₂ and C/O= 1) can reproduce both the relative abundances of CH₃NC and CH₃CN when adopting a branching ratio of 0.8 isomerization for the reaction CH₃⁺ + HCN (9).
5. An elevated C/O ratio (~ 1.0) could also be the key for understanding complex nitrile disk chemistry. Using a fiducial protoplanetary disk astrochemical model, we find that disk observations of CH₃CN and HC₃N are reproduced within an order of magnitude, while our standard model under-predicts the same molecules by 2-3 orders of magnitude.

While the good agreement between observations and models in both a classic PDR and a planet-forming disk, it is important to note that the nitrile grain chemistry is still poorly constrained, and it may contribute to both kinds of regions (e.g. Bertin et al. 2017a,b; Calcutt et al. 2018; Nguyen et al. 2019). Further experiments and theory on nitrile grain surface chemistry and desorption are needed to make progress here. Thus, it would be interesting to add grain chemistry, and in particular grain nitrile chemistry, in the Meudon PDR code to test how the results presented here would be affected. Furthermore, other parameters would be worth testing in future model developments, such as the impact of stellar X-ray irradiation on disk chemistry which could affect its ionization (e.g. Glassgold et al. 1997; Rab et al. 2018; Waggoner & Cleaves 2019), and the sensitivity of disk chemistry to grain sizes (e.g. Wakelam et al. 2019) as smaller grains provide a higher surface area relative to their volume and thus more reaction sites and also tend to have temperatures closer to that of the gas. In the meantime we note that the strong impact of C/O on nitrile chemistry may enable us to use nitriles to constrain this important parameter in disks and PDR analogs.

ACKNOWLEDGMENTS

The authors would like to thank the anonymous referee for constructive suggestions and comments. R. LG. also thanks Tom J. Millar for useful discussion. This work was supported by an award from the Simons Foundation (SCOL # 321183, KO). M. T. B. acknowledges support from the Noland Internship at Caltech.

Software: Pandas (McKinney 2010), Matplotlib (Hunter 2007), NumPy (van der Walt et al. 2011), SciPy (Jones et al. 2001–), Meudon PDR Code (Le Bourlot et al. 1993; Le Petit et al. 2006; Le Bourlot et al. 2012), Nautilus-v1.1 (Hersant et al. 2009; Ruaud et al. 2016; Wakelam et al. 2016).

APPENDIX

A. CRITICAL CHEMICAL REACTIONS ADDED TO THE MEUDON PDR CODE NETWORK

Table A1. Rates of the critical chemical reactions discussed in this study.

Chemical reactions		α ($\text{cm}^3 \text{s}^{-1}$)	β	γ	k rate type ^(a)	T range (K)	Ref. ^(b)	Rate uncertainties ^(c)				
Main formation and destruction pathways for CH_3CNH^+ & CH_3CN												
CH_3^+	HCN	\rightarrow	CH_3CNH^+	$h\nu$	7.20(-9)	-0.50	0.00	(1)	10 – 299	[1], [2]	$F_0 = 10, g = 0$	
CH_3^+	HCN	\rightarrow	CH_3CNH^+	$h\nu$	8.00(-11)	-3.00	0.00	(1)	300 – 800	[2], [3]	$F_0 = 2, g = 0$	
CH_3^+	HNC	\rightarrow	CH_3CNH^+	$h\nu$	9.00(-9)	-0.50	0.00	(1)	10 – 300	[4]	$F_0 = 10, g = 0$	
CH_3CNH^+	e^-	\rightarrow	H	H	H_2CCN	8.00(-8)	-0.50	0.00	(2)	10 – 300	[4]	$F_0 = 3, g = 0$
CH_3CNH^+	e^-	\rightarrow	H	CH_3CN		1.30(-7)	-0.50	0.00	(2)	10 – 300	[4]	$F_0 = 3, g = 0$
CH_3CNH^+	e^-	\rightarrow	HNC	CH_3		6.00(-8)	-0.50	0.00	(2)	10 – 300	[4]	$F_0 = 3, g = 0$
CH_3CNH^+	e^-	\rightarrow	HCN	CH_3		6.00(-8)	-0.50	0.00	(2)	10 – 300	[4]	$F_0 = 3, g = 0$
CH_3CN	$h\nu$	\rightarrow	CN	CH_3		2.95(-9)	0.00	3.07	(3)	–	[5]	$F_0 = 1.3, g = 0$
Main formation and destruction pathways for CH_3NCH^+ & CH_3NC												
CH_3^+	HCN	\rightarrow	CH_3NCH^+	$h\nu$	1.80(-9)	-0.50	0.00	(1)	10 – 299	[1], [2]	$F_0 = 10, g = 0$	
CH_3^+	HCN	\rightarrow	CH_3NCH^+	$h\nu$	2.00(-11)	-3.00	0.00	(1)	300 – 800	[2], [3]	$F_0 = 2, g = 0$	
CH_3NCH^+	e^-	\rightarrow	H	CH_3NC		1.30(-7)	-0.50	0.00	(2)	10 – 300	[4] ^(*)	$F_0 = 3, g = 0$
CH_3NCH^+	e^-	\rightarrow	HCN	CH_3		6.00(-8)	-0.50	0.00	(2)	10 – 300	[4] ^(*)	$F_0 = 3, g = 0$
CH_3NC	$h\nu$	\rightarrow	CN	CH_3		2.95(-9)	0.00	3.07	(3)	–	[5] ^(*)	$F_0 = 1.3, g = 0$
Main formation and destruction pathways for C_3N												
N	c- C_3H	\rightarrow	H	C_3N		1.10(-10)	0.17	0.00	(2)	10 – 300	[4]	$F_0 = 3, g = 0$
C_3N	$h\nu$	\rightarrow	C_2	CN		5.00(-10)	0.00	1.80	(3)	–	[6]	$F_0 = 2, g = 0$
C_3N	O	\rightarrow	CO	CCN		1.00(-10)	0.00	0.00	(2)	10 – 298	[7]	$F_0 = 3, g = 2.97$
C_3N	C	\rightarrow	CN	C_3		2.40(-10)	0.00	0.00	(2)	10 – 300	[4]	$F_0 = 3, g = 0$
Main formation and destruction pathways for HC_3N												
HC_3NH^+	e^-	\rightarrow	H	HC_3N		6.00(-7)	-0.58	0.00	(2)	10 – 800	[8]	$F_0 = 1.4, g = 0$
C_4H	N	\rightarrow	C	HC_3N		7.00(-11)	0.17	0.00	(2)	10 – 300	[4]	$F_0 = 3, g = 0$
C	H_2CCN	\rightarrow	H	HC_3N		1.00(-10)	0.00	0.00	(2)	10 – 300	[4]	$F_0 = 3, g = 0$
N	c- C_3H_2	\rightarrow	H	HC_3N		1.00(-11)	0.00	2000.00	(2)	10 – 800	[8]	$F_0 = 3, g = 500$
C_2H_2	CN	\rightarrow	H	HC_3N		2.72(-10)	-0.52	19.00	(2)	10 – 280	[6]	$F_0 = 1.25, g = 0$
HC_3N	$h\nu$	\rightarrow	CN	C_2H		7.13(-9)	0.00	2.59	(3)	–	[5]	$F_0 = 1.3, g = 0$

NOTE—Numbers in parentheses are power of 10 (a) Rate formulae: (1) Radiative associations and (2) bimolecular gas-phase reactions are computed from the same rate formula $k = \alpha(T/300)^\beta e^{-\gamma/T}$, (3) photo-reactions for which the photo-cross-sections are unknown are computed with $k = \alpha \left(\chi^- e^{-\gamma A_V} + \chi^+ e^{-\gamma(A_V^{\text{max}} - A_V)} \right)$, with χ^- and χ^+ scaling factors of the radiation field with respect to that of Draine on the left and right side of the cloud, respectively (Le Petit et al. 2006); (b) [1] Herbst (1985); [2] Anicich (2003); [3] Harada et al. (2010); [4] Loison et al. (2014); [5] Heays et al. (2017); [6] OSU database; [7] Smith database; [8] Loison et al. (2017); (*) Assumed from the referenced publication; (c) Rate uncertainties are from the KIDA database and are considered to follow a lognormal distribution, i.e. with a probability of $\approx 68\%$ for the rate k to be in the range $\left[\frac{k}{F_0}, k \times F_0 \right]$ and g being an expansion parameter used to parameterize a possible temperature dependence of the uncertainty, according to the formula $F(T) = F_0 \exp\left(g \left| \frac{1}{T} - \frac{1}{T_0} \right| \right)$ with $T_0 = 300$ K (see Wakelam et al. 2012, for more details).

REFERENCES

- Abergel, A., Teyssier, D., Bernard, J. P., et al. 2003, *A&A*, 410, 577
- Andrews, S. M., Rosenfeld, K. A., Kraus, A. L., & Wilner, D. J. 2013, *ApJ*, 771, 129
- Anicich, V. G. 2003, JPL Publication 03-19, 1
- Anicich, V. G., Sen, A. D., Huntress, Wesley T., J., & McEwan, M. J. 1995, *JChPh*, 102, 3256
- Asplund, M., Grevesse, N., Sauval, A. J., & Scott, P. 2009, *ARA&A*, 47, 481
- Beckwith, S. V. W., Sargent, A. I., Chini, R. S., & Guesten, R. 1990, *AJ*, 99, 924
- Bergin, E. A., Du, F., Cleeves, L. I., et al. 2016, *ApJ*, 831, 101
- Bergner, J. B., Guzmán, V. G., Öberg, K. I., Loomis, R. A., & Pegues, J. 2018, *ApJ*, 857, 69
- Bergner, J. B., Öberg, K. I., Bergin, E. A., et al. 2019, *ApJ*, 876, 25
- Bertin, M., Doronin, M., Fillion, J. H., et al. 2017a, *A&A*, 598, A18
- Bertin, M., Doronin, M., Michaut, X., et al. 2017b, *A&A*, 608, A50
- Calcutt, H., Fiechter, M. R., Willis, E. R., et al. 2018, *A&A*, 617, A95
- Cernicharo, J., Kahane, C., Guelin, M., & Gomez-Gonzalez, J. 1988, *A&A*, 189, L1
- Chapillon, E., Dutrey, A., Guilloteau, S., et al. 2012, *ApJ*, 756, 58
- Chiang, E. I., & Goldreich, P. 1997, *ApJ*, 490, 368
- Cleeves, L. I., Bergin, E. A., Qi, C., Adams, F. C., & Öberg, K. I. 2015, *ApJ*, 799, 204
- Cleeves, L. I., Öberg, K. I., Wilner, D. J., et al. 2018, *ApJ*, 865, 155
- Cuadrado, S., Goicoechea, J. R., Pilleri, P., et al. 2015, *A&A*, 575, A82
- Dartois, E., Dutrey, A., & Guilloteau, S. 2003, *A&A*, 399, 773
- Defrees, D. J., McLean, A. D., & Herbst, E. 1985, *ApJ*, 293, 236
- Draine, B. T. 1978, *ApJS*, 36, 595
- Dullemond, C. P., Dominik, C., & Natta, A. 2001, *ApJ*, 560, 957
- Dutrey, A., Guilloteau, S., & Guelin, M. 1997, *A&A*, 317, L55
- Elmegreen, B. G. 2000, *ApJ*, 530, 277
- Fuente, A., Cernicharo, J., Agúndez, M., et al. 2010, *A&A*, 524, A19
- Fuente, A., Rodriguez-Franco, A., Garcia-Burillo, S., Martin-Pintado, J., & Black, J. H. 2003, *A&A*, 406, 899
- Gerin, M., Goicoechea, J. R., Pety, J., & Hily-Blant, P. 2009, *A&A*, 494, 977
- Glassgold, A. E., & Langer, W. D. 1974, *ApJ*, 193, 73
- Glassgold, A. E., Najita, J., & Igea, J. 1997, *ApJ*, 480, 344
- Goicoechea, J. R., Pety, J., Gerin, M., Hily-Blant, P., & Le Boulrot, J. 2009, *A&A*, 498, 771
- Goicoechea, J. R., Pety, J., Gerin, M., et al. 2006, *A&A*, 456, 565
- Gratier, P., Pety, J., Guzmán, V., et al. 2013, *A&A*, 557, A101
- Grenier, I. A., Black, J. H., & Strong, A. W. 2015, *ARA&A*, 53, 199
- Guilloteau, S., Dutrey, A., Piétu, V., & Boehler, Y. 2011, *A&A*, 529, A105
- Guilloteau, S., Reboussin, L., Dutrey, A., et al. 2016, *A&A*, 592, A124
- Guzmán, V., Pety, J., Goicoechea, J. R., Gerin, M., & Roueff, E. 2011, *A&A*, 534, A49
- Guzmán, V. V., Pety, J., Goicoechea, J. R., et al. 2015, *ApJL*, 800, L33
- Habart, E., Abergel, A., Walmsley, C. M., Teyssier, D., & Pety, J. 2005, *A&A*, 437, 177
- Harada, N., Herbst, E., & Wakelam, V. 2010, *Astrophysical Journal*, 721, 1570
- Hartmann, L., Ballesteros-Paredes, J., & Bergin, E. A. 2001, *ApJ*, 562, 852
- Heays, A. N., Bosman, A. D., & van Dishoeck, E. F. 2017, *A&A*, 602, A105
- Henning, T., Semenov, D., Guilloteau, S., et al. 2010, *ApJ*, 714, 1511
- Herbst, E. 1985, *Astrophysical Journal*, 291, 226
- Hersant, F., Wakelam, V., Dutrey, A., Guilloteau, S., & Herbst, E. 2009, *A&A*, 493, L49
- Hogerheijde, M. R., Bergin, E. A., Brinch, C., et al. 2011, *Science*, 334, 338
- Huang, J., Andrews, S. M., Dullemond, C. P., et al. 2018, *arXiv e-prints*, arXiv:1812.04041
- Hunter, J. D. 2007, *Computing in Science Engineering*, 9, 90
- Huntress, W. T., J., & Mitchell, G. F. 1979, *ApJ*, 231, 456
- Indriolo, N., Neufeld, D. A., Gerin, M., et al. 2015, *ApJ*, 800, 40
- Jenkins, E. B. 2009, *ApJ*, 700, 1299
- Jones, A. P., & Ysrad, N. 2019, *arXiv e-prints*, arXiv:1906.01382
- Jones, E., Oliphant, T., Peterson, P., et al. 2001–, *SciPy: Open source scientific tools for Python*, , . <http://www.scipy.org/>
- Kastner, J. H., Qi, C., Gorti, U., et al. 2015, *ApJ*, 806, 75

- Kastner, J. H., Qi, C., Dickson-Vandervelde, D. A., et al. 2018, *ApJ*, 863, 106
- Le Bourlot, J., Le Petit, F., Pinto, C., Roueff, E., & Roy, F. 2012, *A&A*, 541, A76
- Le Bourlot, J., Pineau Des Forets, G., Roueff, E., & Flower, D. R. 1993, *A&A*, 267, 233
- Le Gal, R., Herbst, E., Dufour, G., et al. 2017, *A&A*, 605, A88
- Le Gal, R., Hily-Blant, P., Faure, A., et al. 2014, *A&A*, 562, A83
- Le Gal, R., Öberg, K. I., Loomis, R. A., Pegues, J., & Bergner, J. B. 2019, *ApJ*, 876, 72
- Le Petit, F., Nehmé, C., Le Bourlot, J., & Roueff, E. 2006, *ApJS*, 164, 506
- Le Petit, F., Ruaud, M., Bron, E., et al. 2016, *A&A*, 585, A105
- Loison, J.-C., Wakelam, V., & Hickson, K. M. 2014, *MNRAS*, 443, 398
- Loison, J.-C., Agúndez, M., Wakelam, V., et al. 2017, *MNRAS*, 470, 4075
- Loomis, R., Öberg, K. I., Andrews, S., & et al. 2019, submitted to *ApJ*
- Loomis, R. A., Cleeves, L. I., Öberg, K. I., et al. 2018, *ApJ*, 859, 131
- López, A., Tercero, B., Kisiel, Z., et al. 2014, *A&A*, 572, A44
- Mathis, J. S., Rumpl, W., & Nordsieck, K. H. 1977, *ApJ*, 217, 425
- McKinney, W. 2010, in *Proceedings of the 9th Python in Science Conference*, ed. S. van der Walt & J. Millman, 51 – 56
- Millar, T. J., & Herbst, E. 1990, *MNRAS*, 242, 92
- Millar, T. J., Leung, C. M., & Herbst, E. 1987, *A&A*, 183, 109
- Nath, B. B., & Biermann, P. L. 1994, *MNRAS*, 270, L33
- Nguyen, T., Fourré, I., Favre, C., et al. 2019, *A&A*, 628, A15
- Öberg, K. I., Guzmán, V. V., Furuya, K., et al. 2015, *Nature*, 520, 198
- Patel, B. H., Percivalle, C., Ritson, D. J., Duffy, C. D., & Sutherland, J. D. 2015, *Nature Chemistry*, 7, 301 EP . <https://doi.org/10.1038/nchem.2202>
- Pety, J., Goicoechea, J. R., Hily-Blant, P., Gerin, M., & Teyssier, D. 2007, *A&A*, 464, L41
- Pety, J., Teyssier, D., Fossé, D., et al. 2005, *A&A*, 435, 885
- Pety, J., Gratier, P., Guzmán, V., et al. 2012, *A&A*, 548, A68
- Piétu, V., Dutrey, A., & Guilloteau, S. 2007, *A&A*, 467, 163
- Plessis, S., Carrasco, N., Dobrijevic, M., & Pernot, P. 2012, *Icarus*, 219, 254
- Plessis, S., Carrasco, N., & Pernot, P. 2010, *JChPh*, 133, 134110
- Powner, M. W., Gerland, B., & Sutherland, J. D. 2009, *Nature*, 459, 239 EP . <http://dx.doi.org/10.1038/nature08013>
- Przybilla, N., Nieva, M.-F., & Butler, K. 2008, *ApJL*, 688, L103
- Qi, C., Öberg, K. I., Wilner, D. J., & Rosenfeld, K. A. 2013, *ApJL*, 765, L14
- Rab, C., Güdel, M., Woitke, P., et al. 2018, *A&A*, 609, A91
- Remijan, A. J., Hollis, J. M., Lovas, F. J., Plusquellic, D. F., & Jewell, P. R. 2005, *ApJ*, 632, 333
- Rimmer, P. B., Herbst, E., Morata, O., & Roueff, E. 2012, *A&A*, 537, A7
- Rosenfeld, K. A., Andrews, S. M., Wilner, D. J., Kastner, J. H., & McClure, M. K. 2013, *ApJ*, 775, 136
- Ruaud, M., Wakelam, V., & Hersant, F. 2016, *MNRAS*, 459, 3756
- Shakura, N. I., & Sunyaev, R. A. 1973, *A&A*, 24, 337
- Sutherland, J. D. 2016, *Angewandte Chemie International Edition*, 55, 104. <https://onlinelibrary.wiley.com/doi/abs/10.1002/anie.201506585>
- van der Walt, S., Colbert, S. C., & Varoquaux, G. 2011, *Computing in Science and Engineering*, 13, 22
- van Dishoeck, E. F., & Blake, G. A. 1998, *ARA&A*, 36, 317
- Vasyunin, A. I., Semenov, D., Henning, T., et al. 2008, *ApJ*, 672, 629
- Vasyunin, A. I., Sobolev, A. M., Wiebe, D. S., & Semenov, D. A. 2004, *Astronomy Letters*, 30, 566
- Vigren, E., Kamińska, M., Hamberg, M., et al. 2008, *Physical Chemistry Chemical Physics (Incorporating Faraday Transactions)*, 10, 4014
- Wagenblast, R., & Hartquist, T. W. 1989, *MNRAS*, 237, 1019
- Waggoner, A. R., & Cleeves, L. I. 2019, arXiv e-prints, arXiv:1908.08048
- Wakelam, V., Chaietillon, E., Dutrey, A., et al. 2019, *MNRAS*, 484, 1563
- Wakelam, V., Herbst, E., Le Bourlot, J., et al. 2010, *A&A*, 517, A21
- Wakelam, V., Herbst, E., & Selsis, F. 2006, *A&A*, 451, 551
- Wakelam, V., Ruaud, M., Hersant, F., et al. 2016, *A&A*, 594, A35
- Wakelam, V., Selsis, F., Herbst, E., & Caselli, P. 2005, *A&A*, 444, 883
- Wakelam, V., Herbst, E., Loison, J. C., et al. 2012, *ApJS*, 199, 21
- Whittet, D. C. B. 2010, *ApJ*, 710, 1009
- Williams, J. P., & Best, W. M. J. 2014, *ApJ*, 788, 59